

# Characterization of MIPS $70\mu\text{m}$ flux non-linearity

Roberta Paladini & Alberto Noriega-Crespo

April 22, 2009

## 1. Summary

This document describes the work undertaken for characterizing the flux non-linearity of the MIPS  $70\mu\text{m}$  array. The effect, due to the change of rate of incident radiation on the detector, has been described in Gordon et al. (2007) and is typical of Ge:Ga photoconductors. The analysis has made use of MIPS calibration data acquired in Wide Field (WF), Narrow Field (NF) and Spectral Energy Distribution (SED) mode, and has attempted the characterization of this effect in terms of flux density as well as of surface brightness. Indications of a departure from a linear behaviour are present in both cases. The analysis shows that the NF measurements are less severely affected by a non-linear behaviour with respect to WF observations. In particular, the MIPS  $70\mu\text{m}$  NF data of targets brighter than  $\sim 2$  Jy underestimate the true flux up to 20%, while WF measurements underestimate the true flux up to 50%. A functional form characterizing the non-linear behaviour of the NF and WF measurements is provided. We have also rederived the calibration factor for NF, before and after applying the non-linearity correction described above. For this purpose we make use of a data set of calibration stars which nearly doubles the sample in Gordon et al. (2007). The calibration factor obtained before correcting for non-linearity effects is consistent with Gordon et al. (2007). However, when non-linearity effects are taken into account, we show that the calibration factor is lower by  $\sim 20\%$ .

## 2. Method

In order to characterize the non-linear behaviour of the array, we have analyzed the calibration (WF, NF and SED) data of bright (meaning  $S_{70\mu\text{m}} > 1$  Jy) stars and asteroids, acquired by MIPS over the entire duration of the cryogenic mission. A summary of these data is given in Table 1, 2 and 3. The sources cover the flux range 2 - 20 Jy. No star/asteroid brighter than 20 Jy at  $70\mu\text{m}$  is known to exist. This sets an upper flux limit up to which the study can be conducted. The underlying assumption of the investigation is that the MIPS  $70\mu\text{m}$  array, in SED mode, is characterized by a linear response up to at least 20 Jy, hence providing a reliable estimate of the *true* flux (see also Lu et al. (2008)). In some cases (mainly stars), multiple observations in the same mode (WF, NF, SED) have been acquired. For these, data for the same mode have been appropriately combined. At this stage, the WF data for all the stars and asteroids are compared to the corresponding SED data. Likewise for NF data. A fit to the distribution so obtained provides information on the departure of the WF and NF observed fluxes from the *true* flux for each value in the considered flux range (i.e. 2 - 20 Jy).

We have proceeded along the same lines for studying the behaviour in terms of surface brightness. In this case, a pixel-to-pixel comparison of the WF and NF data has been performed, with the resulting best-fit function providing indication of the non-linearity of the array in these observing modes. While the main body of the document will focused on integrated fluxes, the discussion related to surface brightness will be addressed in a dedicated section (Sect. 6).

### 3. Data sample and Analysis - stars

For each star in Table 1, we have analyzed the WF, NF and SED data. The WF, NF and SED data have not been necessarily acquired during the same MIPS observational campaign, given that the flux of the star is supposed not to vary in time. The data obtained in SED mode with a 3-sec integration are affected by a latency effect, with the consequence that the integrated flux of the source is enhanced by a factor which varies depending on the flux itself. For this reason, we have decided not to include in the present study the 3-sec SED data. All the SED data reported here refer to 10-sec observation cycles.

The analysis of the WF, NF and SED data has required some reprocessing. As described in Gordon et al. (2007), in WF mode the source is dithered around the array to ensure that its flux is collected in the fast response regime. However, the dithering causes the source background to be in the slow response, resulting in a drifting background signal. To correct for this effect, one needs to correct the WF BCDs first by applying a column filter, then a time filter. The NF mode is relatively simpler to treat, as no dithering is involved, rather a chopping of the array on and off the source. In this case, to remove the effect of a drifting background, it is enough to subtract pairs of on/off positions.

Once the WF and NF BCDs have been corrected and mosaiced, the integrated flux of each source has been derived using two techniques: aperture photometry and PSF fitting. Aperture photometry has been performed by adding the flux in a circular aperture of  $35''$ , after estimating and subtracting the background in a sky aperture defined by radii of  $39''$  and  $65''$ . Aperture corrections of 1.185 and 1.181, for WF and NF respectively, have also been applied. In the case of the PSF fitting, for NF we have used a blue PRF (Point Response Function) obtained by combining all the archival data for one of the bright calibrators (HD045348). Such a PRF performs significantly better, in terms of residuals, than the nominal blue PRF provided by the SSC. For WF, we have instead made use of the nominal PRF, since a PRF built with the WF data of HD045348 retrieves residuals comparable to the nominal one.

The SED data also necessitate of some level of reprocessing. This is due to the fact that the current Spitzer pipeline does not mosaic the SED BCDs with the correct pmask bits setting. Therefore, for each data set the SED mosaic has been regenerated with Mopex, and the spectrum extracted using a 5-column aperture. In addition, in order to compare the  $70\mu\text{m}$  flux obtained from the the WF and NF measurements with the one derived from the SED mode, we have integrated the SED spectrum using the MIPS bandpass filter.

The final stage of this part of the analysis consists in checking if multiple observations in the same mode are available for a given source. In this case, we combine these data with a weighted mean.

Plots of the WF and NF averaged fluxes for each star versus the SED reference fluxes have been made, both for aperture photometry and PSF fitting (see Fig. 1 and 2). The resulting distributions have been fitted with a straight line as well as with a power-law. The best-fits are shown in the figures.

### 4. Data sample and Analysis - asteroids.

For each source in Table 3, we have analyzed the WF, NF and SED data. With respect to stars, in this case data taken with different observing modes but for the same source must have been acquired during the same MIPS campaign. This is because the observed flux can change up to a factor 2 from one campaign to another, as a result of the rotation of the

Table 1: WF/NF data for bright stars.  $70\mu\text{m}$  fluxes are from Lu et al. (2008) when available, otherwise from Gordon et al. (2007).

<i>Source</i>	AOR ID	Type	Campaign	Proc.	Ver.	Flux Jy		
HD006860	11893504	WF	12	S16.1.0		5.47		
	28256768	WF	55	S18.1.0				
	20406272	NF	34	S16.1.0				
	28257024	NF	55	S18.1.0				
HD018884	11894016	WF	12	S16.1.0		4.96		
	28257536	WF	55	S18.1.0				
	28257792	NF	55	S18.1.0				
HD029139	13315072	WF	19	S16.1.0		13.13		
	24081408	WF	44	S16.1.0				
	24312576	WF	45	S16.1.0				
	28256000	WF	55	S18.1.0				
	28423168	WF	56	S18.1.0				
	13311232	NF	19	S16.0.1				
	24081664	NF	44	S16.1.0				
	24312832	NF	45	S16.1.0				
	28256256	NF	55	S18.1.0				
	28423424	NF	56	S18.1.0				
	HD034029	12064512	WF	13	S16.1.0			2.91
		16988416	WF	30	S16.0.1			
28423936		WF	56	S18.1.0				
17043712		NF	30	S16.0.1				
28424192		NF	56	S18.1.0				
HD045348	24485120	WF	46	S16.1.0		2.96		
	24652032	WF	47	S17.0.4				
	24832768	WF	48	S17.0.4				
	24984320	WF	49	S17.0.4				
	25136384	WF	50	S17.2.0				
	27412736	WF	51	S17.2.0				
	24485376	NF	46	S16.1.0				
	24652288	NF	47	S17.0.4				
	24833024	NF	48	S17.0.4				
	24984576	NF	49	S17.0.4				
	25136640	NF	50	S17.2.0				
27412992	NF	51	S17.2.0					
HD108903	13112832	WF	18	S16.1.0		19.08		
	23914240	WF	43	S16.1.0				
	27877120	WF	53	S18.1.0				
	28027136	WF	54	S18.1.0				
	13113600	NF	18	S16.1.0				
	23914752	NF	43	S16.1.0				
	27877376	NF	53	S18.1.0				
28027392	NF	54	S18.1.0					

Table 1 - continued

<i>Source</i>	AOR	Type	Campaign	Proc.	Ver.	Flux Jy
HD124897	23914496	WF	43	S16.1.0		14.32
	24833280	WF	48	S17.0.4		
	24984832	WF	49	S17.0.4		
	27877632	WF	53	S18.1.0		
	28027904	WF	54	S18.1.0		
	23915008	NF	43	S16.1.0		
	24833536	NF	48	S17.0.4		
	24985088	NF	49	S17.0.4		
	27877888	NF	53	S18.1.0		
	28028160	NF	54	S18.1.0		
HD217906	11784192	WF	11	S16.1.0		5.42
	12868608	NF	16	S16.1.0		

asteroid in space.

The reprocessing of the WF, NF and SED data has been conducted following the same lines described in Sect. 3. Likewise, fluxes have been estimated using aperture photometry and PSF fitting. We have used the aperture corrections at 60K provided in Gordon et al. (2007), equal to 1.24 and 1.22 for WF and NF, respectively. For PSF fitting of NF data, the PRF obtained from HD045348 has been adopted, resulting in surprisingly good residuals, i.e. comparable with the r.m.s of the background in the sky annulus (see Fig. 3 and Table 4).

On the contrary, for WF we have used the nominal PRF provided by the SSC. Plots of the WF and NF fluxes for each asteroid versus the SED reference fluxes have been made, both for aperture photometry and PSF fitting (see Fig. 4 and 5). The distributions have been fitted with a straight line as well as with a power-law. The best-fits are illustrated in the figures.

## 5. Results - integrated flux

The individual samples for the integrated flux of stars and asteroids are combined into a single sample, and the WF/NF versus SED values distributions are plotted. A fit to the data is performed, using both a straight line and a power-law. The results are shown in Fig. 6 and 7. These are consistent with the findings of the analysis for stars and asteroids only. In WF mode, the non-linear behaviour of the MIPS  $70\mu\text{m}$  array results in observed fluxes depressed of  $\sim 30\%$  -  $50\%$  with respect to the *true* fluxes, depending on the method adopted for performing the photometric measurements (aperture photometry or PSF fitting). The NF mode appears to be less severely affected by non-linearity effects. In this case, the observed fluxes are depressed by 10% and 20%, respectively. Also, a power-law characterization of the non-linear behaviour does not seem to be strongly favored by the observations, suggesting that the best-fit parameters of the straight-lines given in Fig. 6 and 7 can be used to efficiently correct the data.

Table 2: SED data for bright stars.  $70\mu\text{m}$  fluxes are, when available, from SED measurements reported in Lu et al. (2008), otherwise from Gordon et al. (2007).

<i>Source</i>	AOR	Campaign	Proc.	Ver.	Flux Jy		
HD006860	15811840	24	S16.1.0		5.47		
	28257280	55	S18.1.0				
HD018884	13124352	18	S16.1.0		4.96		
	28258048	55	S18.1.0				
HD029139	13309440	19	S16.1.0		13.13		
	28256512	55	S18.1.0				
	28423680	56	S18.1.0				
HD034029	28424448	56	S18.1.0		2.91		
HD045348	13124608	18	S16.1.0		2.96		
	13309952	19	S16.1.0				
	13615872	21	S16.1.0				
	15992832	25	S16.1.0				
	16229376	26	S16.1.0				
	16377600	27	S16.1.0				
	16839680	29	S16.1.0				
	20912896	37	S16.1.0				
	21062656	38	S16.1.0				
	24485888	46	S16.1.0				
	HD108903	13123840	18	S16.1.0			19.08
		13309184	19	S16.1.0			
15248640		22	S16.1.0				
15422720		23	S16.1.0				
16839424		29	S16.1.0				
21203968		39	S16.1.0				
27878144		53	S18.1.0				
28027648		54	S18.1.0				
HD124897	11625216	10	S16.1.0		14.32		
	13124096	18	S16.1.0				
	15248896	22	S16.1.0				
	15422976	23	S16.1.0				
	27878400	53	S18.1.0				
	28028416	54	S18.1.0				
HD217906	12881920	16	S16.1.0		5.42		

Table 3: WF/NF/SED data for bright asteroids.  $70\mu\text{m}$  fluxes are the values measured in SED mode during the observational campaign indicated in the table.

<i>Source</i>	AOR	Type	Campaign	Proc.	Ver.	Flux Jy
Isis	27658496	WF	52	S18.1.0		5.5
	27658752	NF	52	S18.1.0		
	27659008	SED	52	S18.1.0		
Lacadiera	29676800	WF	59	S18.5.0		5.35
	29677056	NF	59	S18.5.0		
	29677312	SED	59	S18.5.0		
Massalia	28473600	WF	56	S18.1.0		6.23
	28473344	NF	56	S18.1.0		
	28473856	SED	56	S18.1.0		
Roberta	28070400	WF	54	S18.1.0		13.56
	28070144	NF	54	S18.1.0		
	28070656	SED	54	S18.1.0		
Sappho	28724224	WF	58	S18.5.0		2.17
	28724480	NF	58	S18.5.0		
	28724736	SED	58	S18.5.0		

Table 4: Residuals of NF PSF fitting for bright asteroids.

<i>Source</i>	$\text{rms}_{sky}$	$\text{rms}_{source}$	S/N
Isis	0.0014	0.0021	1.5
Lacadiera	0.0013	0.0019	1.5
Massalia	0.0019	0.0027	1.4
Roberta	0.0025	0.0053	2
Sappho	0.0017	0.0013	0.8

## 6. Results - surface brightness

For each source in Table 1 and 3, we have also produced surface brightness distribution plots using the WF and NF data. These have been reprocessed according to the guidelines described in Sect. 2. In addition, to account for the different angular resolution, we have applied a smoothing box to the NF data. For the brightest object of the sample (the star HD108903), we reach a maximum surface brightness of 1300 MJy/sr (Fig. 8). A functional form (straight line and power-law) is fitted to the distribution. Fig. 8 shows that the result is in agreement with what found for the case of the integrated flux, taking into account that the NF data are off by  $\sim 20\%$  with respect to the *true* surface brightness. In addition, the figure also emphasizes that the effect does not depend on the time of observation, given that the functional form fitted through the data is basically the same regardless of the MIPS campaign. The scatter visible in the plots can be explained as due to residual background drifting not corrected by the column and time filtering.

## 7. Non-linearity and NF calibration factor

As part of the non-linearity study, we have rederived the calibration factor for NF, and investigated how this is affected by the non-linearity correction. For this purpose, we have made use of the calibration data provided in Table 6. Remarkably, the sample of stars shown in the table nearly doubles the number of sources used in Gordon et al. (2007).

The data processing follows the lines described in Sect. 3 and consists in the subtraction of the on/off position. For each set of data, the calibration factor is estimated by dividing the observed  $70\mu\text{m}$  flux by the predicted flux and pixel size (in steradian). The predicted flux, for each calibration star, is taken from Gordon et al. (2007), and it is computed using the appropriate Kurucz (1993) model, as discussed in Engelbracht et al. (2006). The calibration factors obtained for the same star and different campaigns are weighted-averaged, in order to have, for a given star, a unique value of calibration factor and corresponding uncertainty. The observed  $70\mu\text{m}$  fluxes have been derived with aperture photometry and psf fitting (see Fig.9, top and bottom panels). As in Sect. 3, for aperture photometry we have added the flux within a circular aperture of radius  $35''$ , after estimating and subtracting the background in a sky aperture of radii  $39''$  and  $65''$ , respectively; in the case of PSF fitting we have used the same PRF (obtained by combining NF calibration data for HD045348) as in the non-linearity study.

After deriving a value for the calibration factor for each star in Table 6, we fit the Calibration Factor vs. Flux distribution, as shown in Fig. 9. The best-fit values are provided in the plots. We notice a discrepancy of order of 10% between the final calibration factor estimated from aperture photometry and the one obtained from PSF fitting, although both values appear to be consistent with Gordon et al. (2007).

We then apply to the data the non-linearity correction derived in Sect. 5, and re-compute the calibration factor. We apply the correction retrieved from the NF sample of calibration stars and asteroids, for the case of PSF fitting (Fig. 7, bottom panel). The correction is applied, for each star and observational campaign, to the mosaic obtained after the on/off subtraction. The calibration factor is then re-calculated, by using aperture photometry and PSF fitting, with the same procedure as described above. The result is illustrated in Fig. 10 (top and bottom panel). Clearly (and as expected) the calibration factor appears to be decreased by  $\sim 20\%$ , i.e. of the same order of magnitude of the applied non-linearity correction .

## 7. References

Table 6: NF data of calibration stars used to derive the calibration factor.  $70\mu\text{m}$  fluxes are the predicted values from Gordon et al. (2007).

<i>Source</i>	AOR	Campaign	Proc.	Ver.	Flux Jy
HD006860	20406272	34	S16.1.0		5.334±0.202
	28257280	55	S18.1.0		
HD018884	28258048	55	S18.1.0		4.645±0.160
	28985344	59	S18.5.0		
	31911680	60	S18.7		
HD024512	20415232	35	S16.0.1		2.421±0.094
HD029139	13309440	19	S16.1.0		12.840±0.451
	24081664	44	S16.1.0		
	24312832	45	S16.1.0		
	28256512	55	S18.1.0		
	28423680	56	S18.1.0		
HD034029	17043712	30	S16.1.0		5.095±0.201
	28424448	56	S18.1.0		
	28584192	57	S18.1.0		
	31912448	60	S18.7.0		
HD045348	9456384	6	S16.1.0		3.0.85±0.067
	24485888	46	S16.1.0		
	24652288	47	S17.0.4		
	24833024	48	S17.0.4		
	24984576	49	S17.0.4		
	25136640	50	S17.2.0		
	27412992	51	S17.2.0		
HD048915	9456896	6	S16.1.0		2.900±0.354
	21407232	40	S16.0.1		
HD050310	21207040	39	S16.1.0		0.706±0.0204
HD071129	16863744	29	S16.1.0		5.153±0.168
HD080493	13635072	21	S16.1.0		1.686±0.06
HD082668	9652992	7	S16.1.0		1.424±0.204
HD100029	9189888	5	S16.1.0		1.124±0.038
HD108903	13123840	18	S16.1.0		17.000±1.766
	19482624	33	S16.1.0		
	23914752	43	S16.1.0		
	27878144	53	S18.1.0		
	28027648	54	S18.1.0		
HD124897	19482880	33	S16.1.0		14.340±0.778
	23601664	42	S16.1.0		
	23915008	43	S16.1.0		
	24833536	48	S17.0.4		
	24985088	49	S17.0.4		
	27878400	53	S18.1.0		
	28028416	54	S18.1.0		

Table 6 - continued

<i>Source</i>	AOR	Campaign	Proc.	Ver.	Flux Jy
HD131873	9190400	5	S16.1.0		3.363±0.123
	21620736	41	S16.1.0		
	24651776	47	S17.0.4		
	24832512	48	S17.0.4		
	24984064	49	S17.0.4		
	25136128	50	S17.2.0		
	27412480	51	S17.2.0		
	27657728	52	S18.1.0		
	28583424	57	S18.1.0		
	28725248	58	S18.5.0		
HD163588	9942784	9	S16.1.0		0.354±0.009
HD164058	13802240	21	S16.1.0		3.315±0.099
HD217906	12881920	16	S16.1.0		7.348±0.273
	28726016	58	S18.5.0		
	28984576	59	S18.5.0		

Engelbracht, C. W., Blaylock, M., Su, K. Y. L., et al., 2007, PASP, 119, 994  
Gordon, K. D., Engelbracht, C. W., Fadda, D., et al., 2007, PASP, 119, 1019  
Kurucz, R. L., 1993, VizieR Online Data Catalog, 6039, 0  
Lu, N., Smith, P., Engelbracht, C. W., et al., 2008, PASP, 120, 328

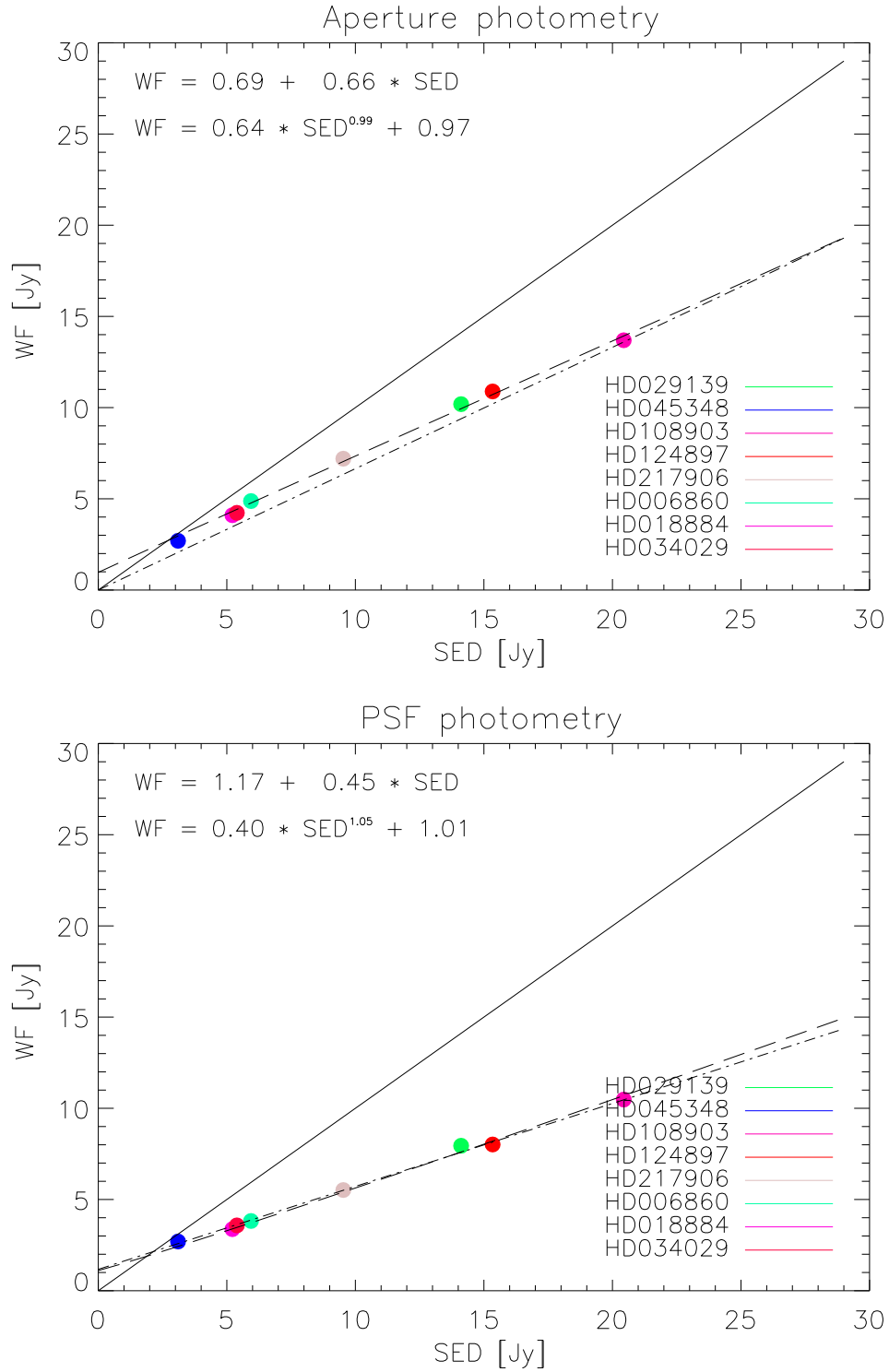


Figure 1: WF vs. SED flux density values for the sample of bright stars. Top panel: NF fluxes are measured with aperture photometry. Bottom panel: WF fluxes are measured with PSF fitting. Both panels: solid line denotes one-to-one correlation; dash-dotted line denotes fit with a straight line; dashed line denotes fit with a power-law.

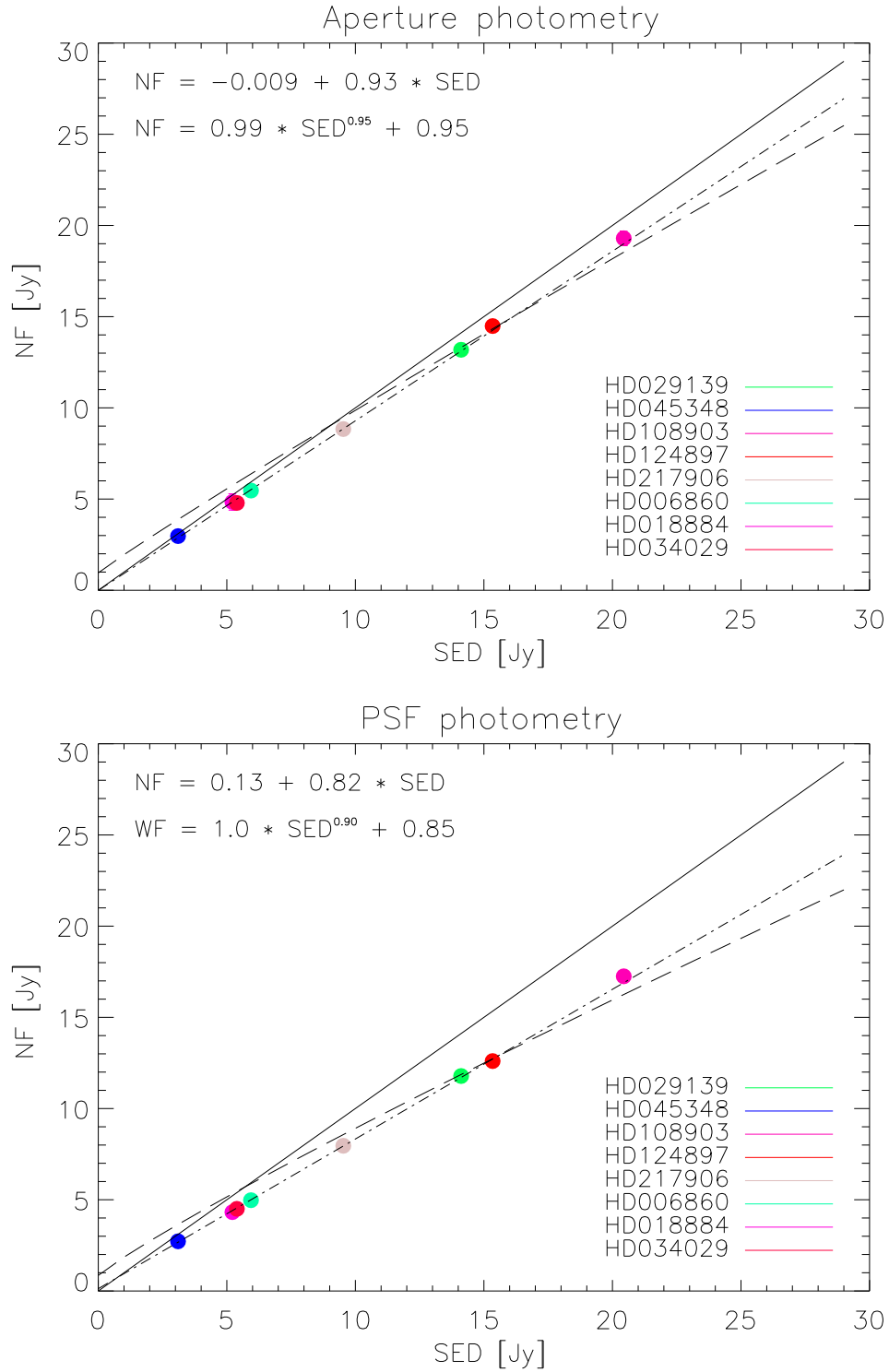


Figure 2: NF vs. SED flux density values for the sample of bright stars. Top panel: WF fluxes are measured with aperture photometry. Bottom panel: NF fluxes are measured with PSF fitting. Notation of lines as in Fig. 1.

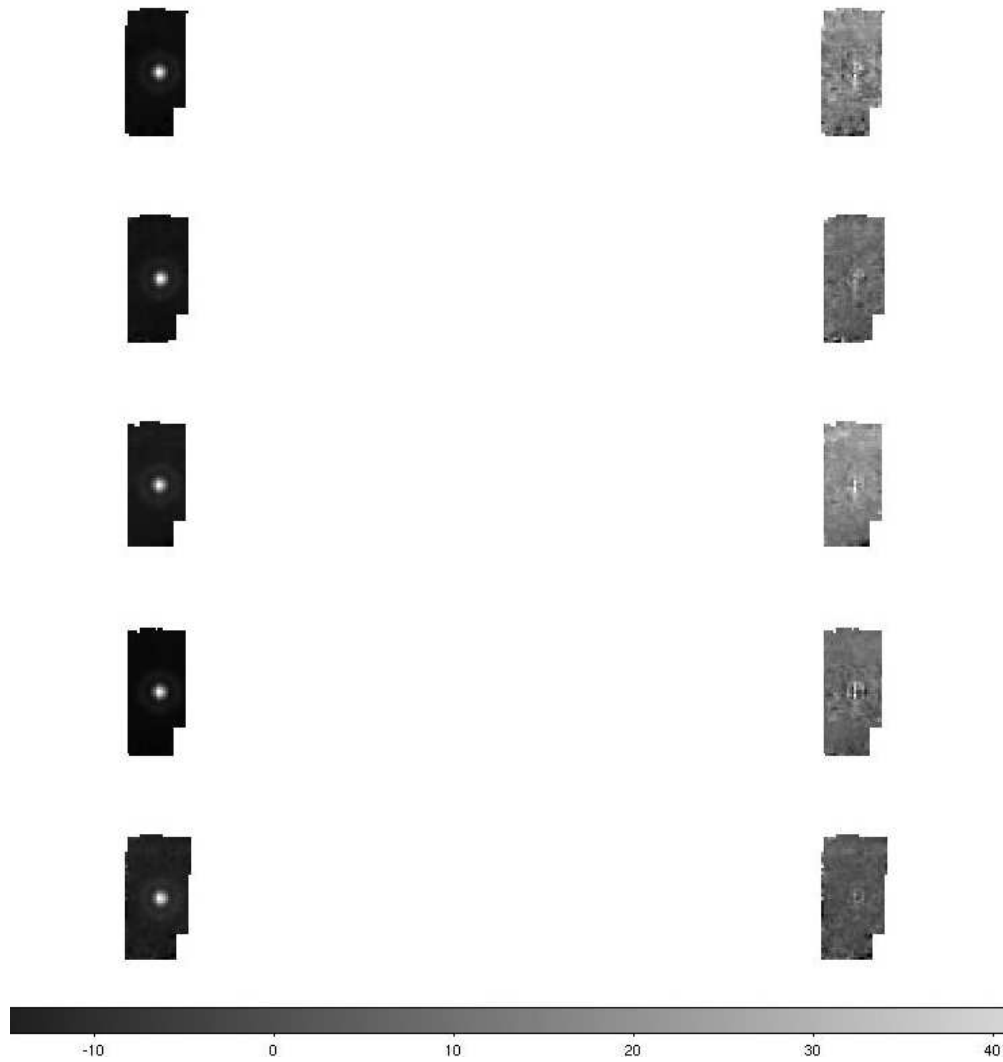


Figure 3: NF mosaics of the asteroids sample with the corresponding residuals. From top to bottom: Isis, Lacadiera, Massalia, Roberta, Sappho.

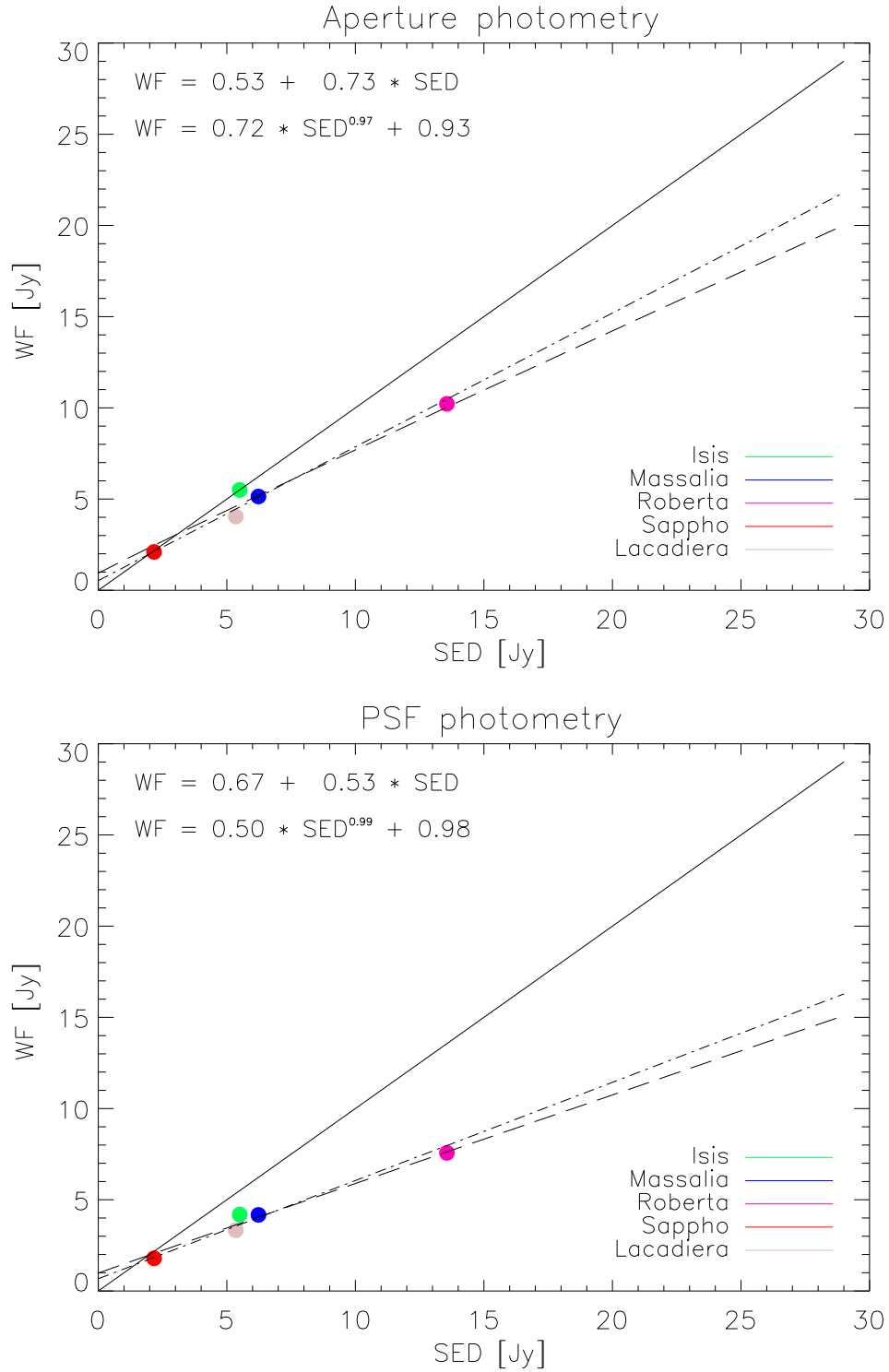


Figure 4: WF vs. SED flux density values for the sample of bright asteroids. Top panel: NF fluxes are measured with aperture photometry. Bottom panel: WF fluxes are measured with PSF fitting. Notation of lines as in Fig. 1.

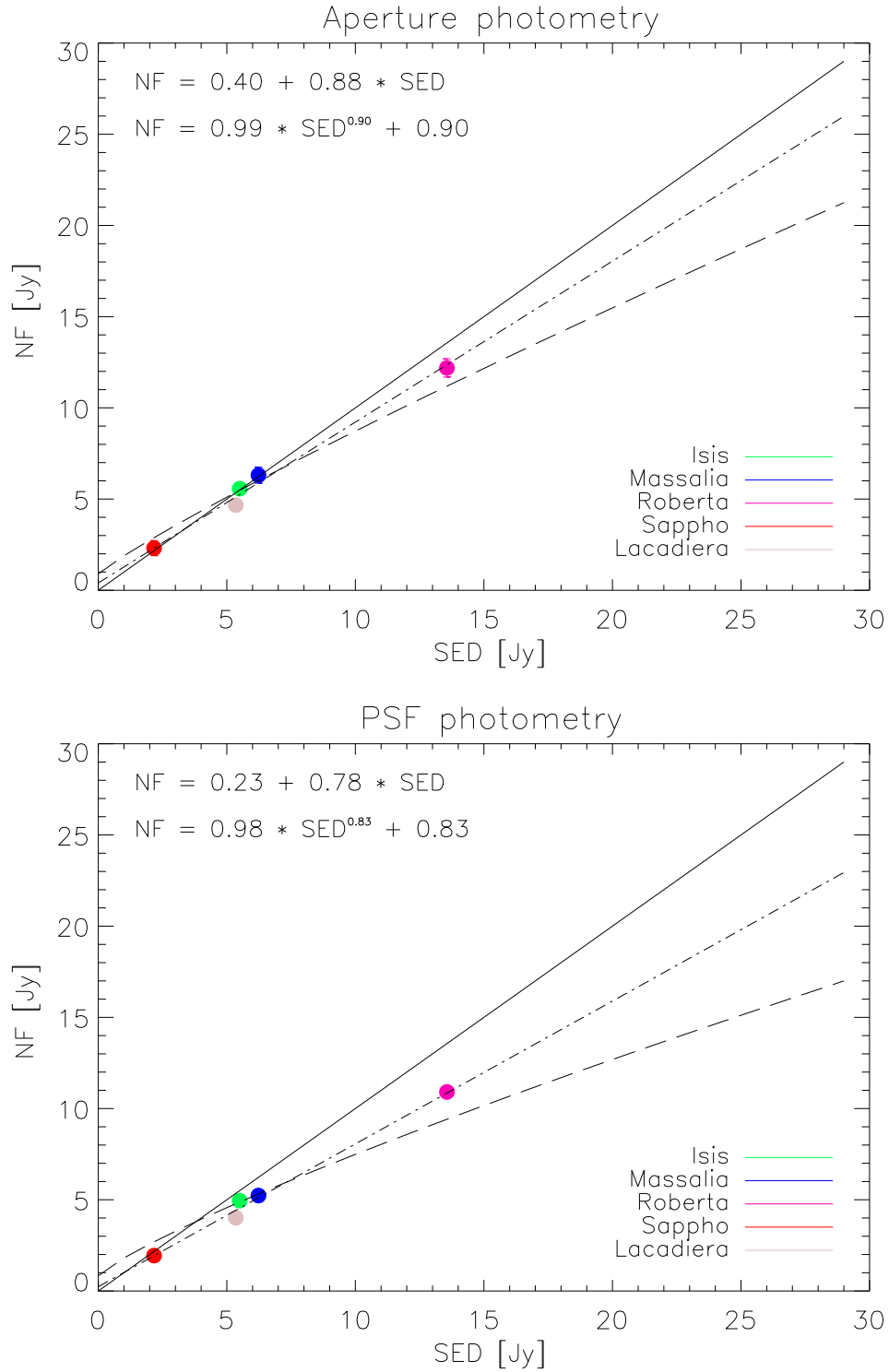


Figure 5: NF vs. SED flux density values for the sample of bright asteroids. Top panel: WF fluxes are measured with aperture photometry. Bottom panel: NF fluxes are measured with PSF fitting. Notation of lines as in Fig. 1.

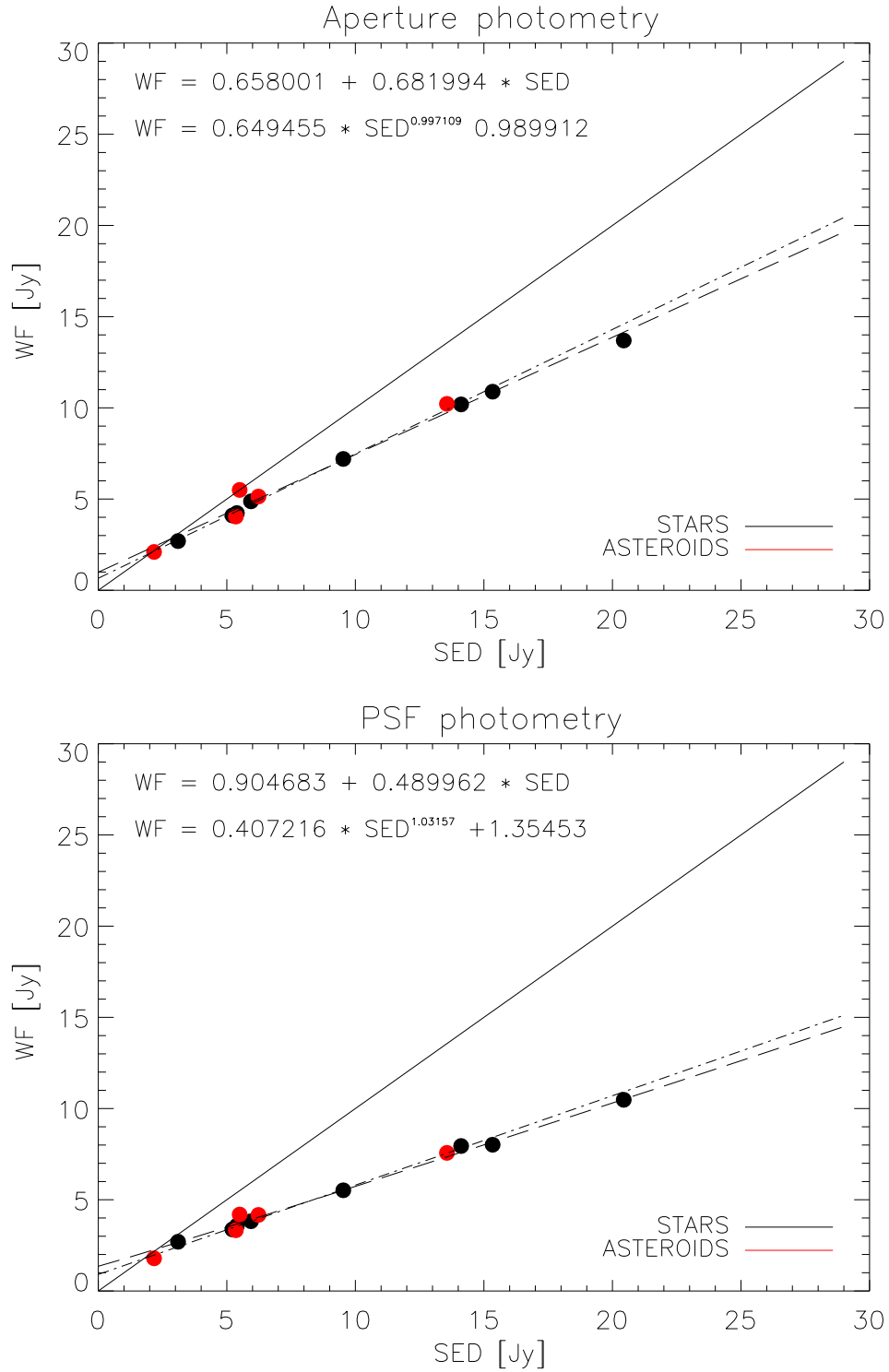


Figure 6: WF vs. SED flux density values for a combined sample of stars and asteroids. Top panel: NF fluxes are measured with aperture photometry. Bottom panel: WF fluxes are measured with PSF fitting. Notation of lines as in Fig. 1.

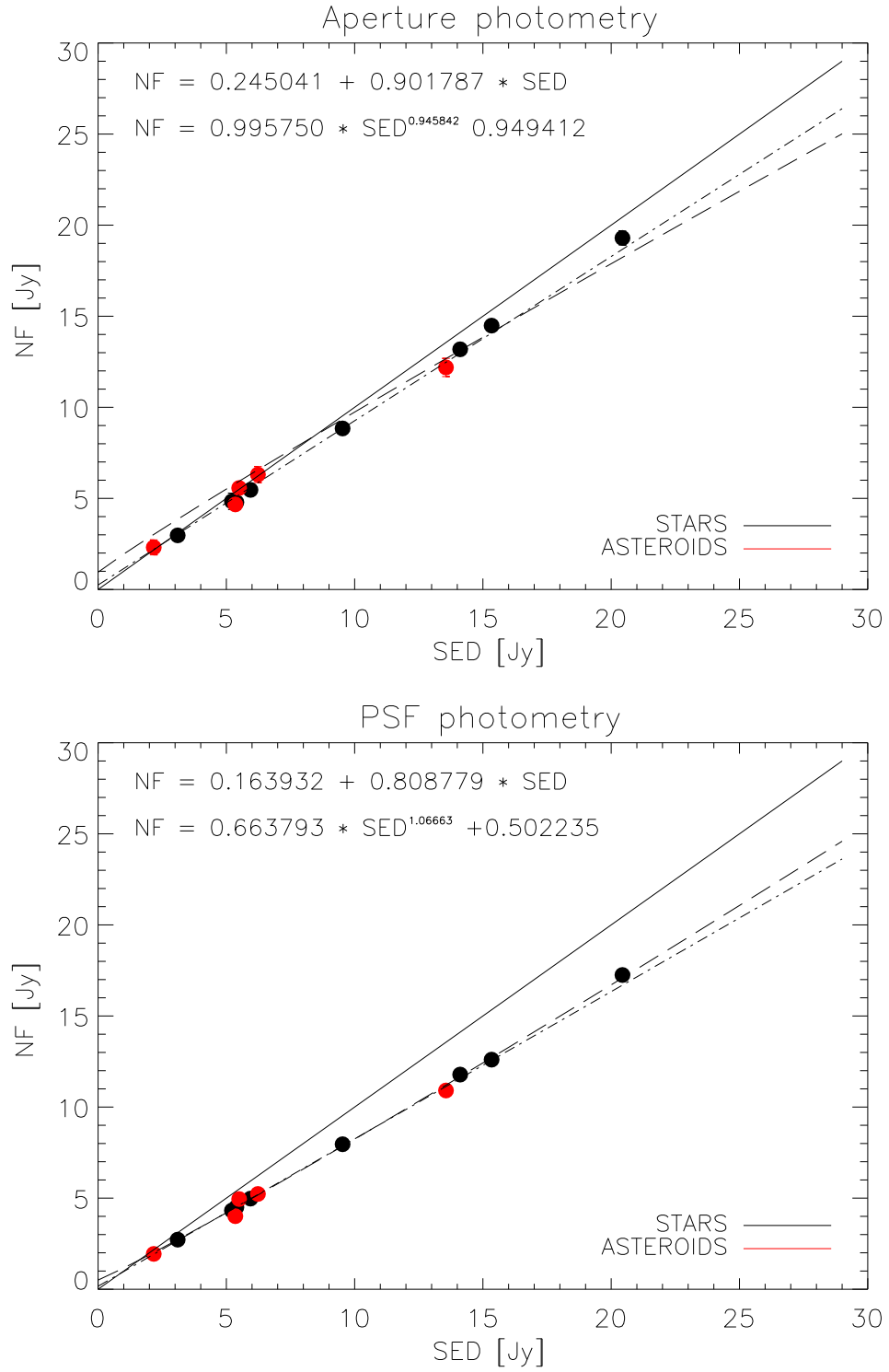


Figure 7: NF vs. SED flux density values for a combined sample of stars and asteroids. Top panel: WF fluxes are measured with aperture photometry. Bottom panel: NF fluxes are measured with PSF fitting. Notation of lines as in Fig. 1.



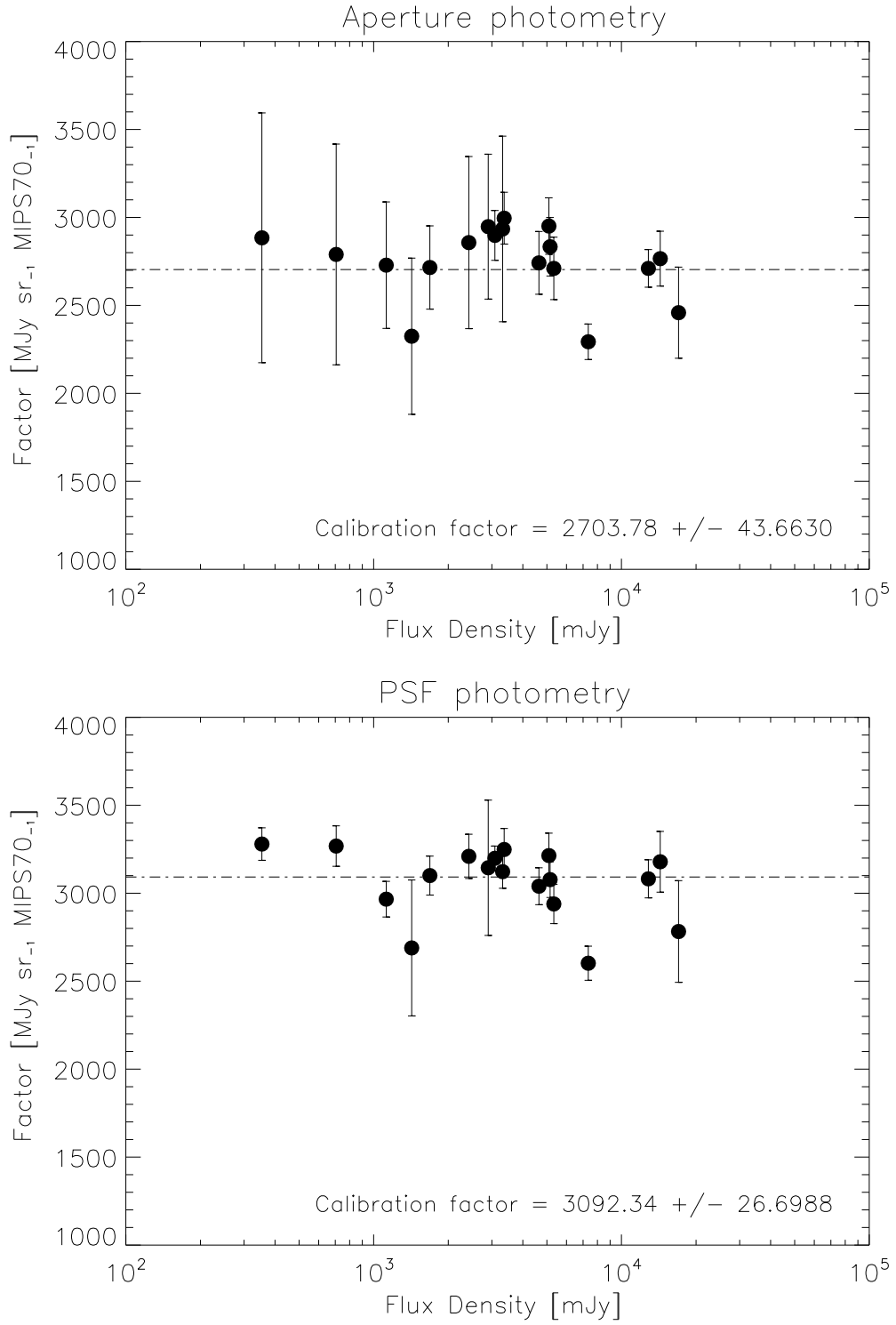


Figure 9: NF calibration factor derived from the calibration stars in Table 6. Top panel: fluxes are measured with aperture photometry. Bottom panel: NF fluxes are measured with PSF fitting.

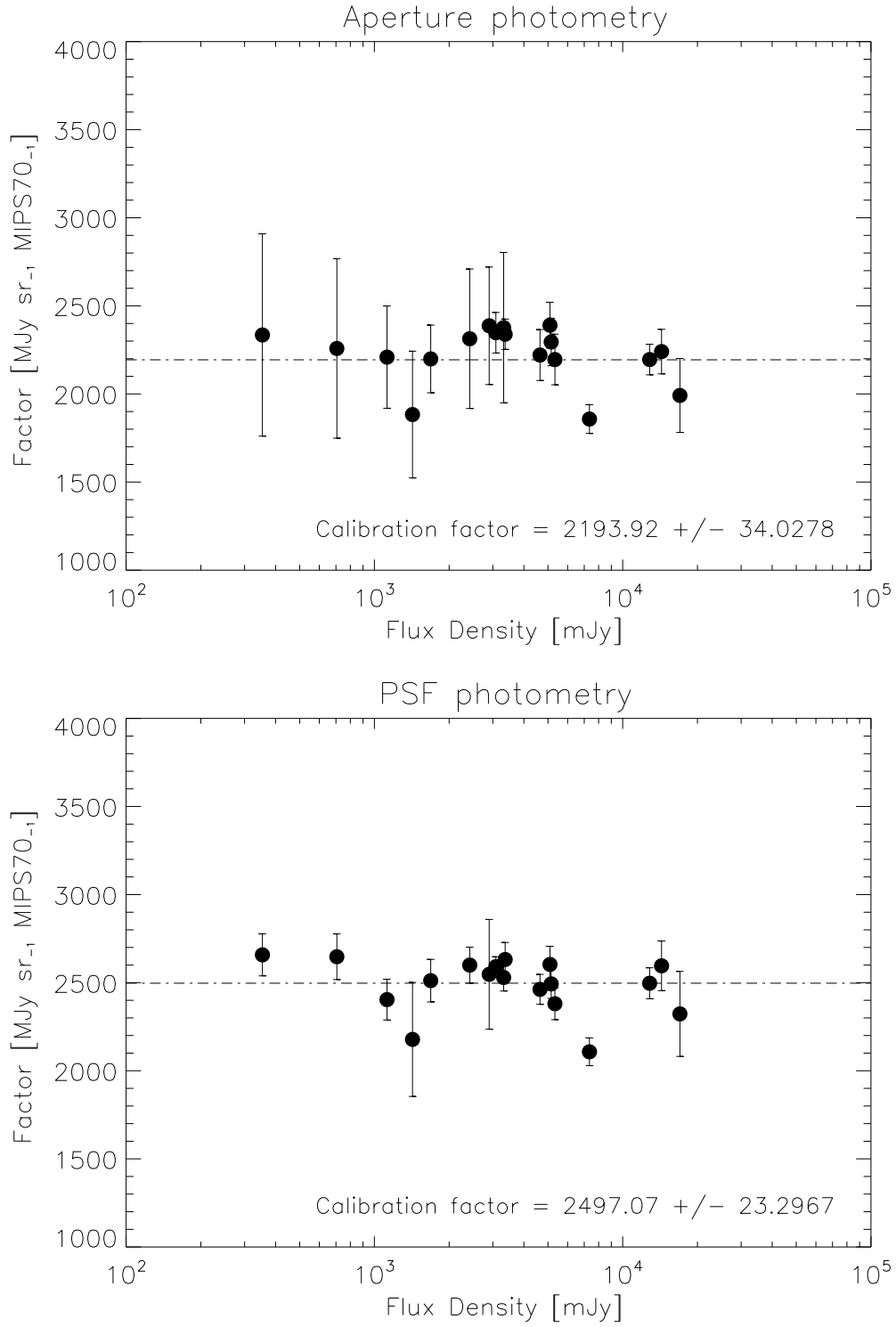


Figure 10: NF calibration factor rederived after application of the non-linearity correction as in eq. ( ) and Figure 7 (bottom). Top panel: fluxes are measured with aperture photometry. Bottom panel: NF fluxes are measured with PSF fitting.